



## Article

# An Integrated Approach for 3D Solar Potential Assessment at the City Scale

Hassan Waqas <sup>1</sup>, Yuhong Jiang <sup>2,\*</sup>, Jianga Shang <sup>1,2</sup>, Iqra Munir <sup>3</sup> and Fahad Ullah Khan <sup>4</sup>

<sup>1</sup> National Engineering Research Center for Geographic Information System, School of Geography, China University of Geosciences, Wuhan 430074, China; waqashassan@cug.edu.cn (H.W.); jgshang@cug.edu.cn (J.S.)

<sup>2</sup> School of Computer Science, China University of Geosciences, Wuhan 430074, China

<sup>3</sup> State Key Laboratory of Information Engineering in Surveying, Mapping, and Remote Sensing (LIESMARS), Wuhan University, Wuhan 430079, China

<sup>4</sup> School of Civil and Environmental Engineering, University of Engineering and Technology, Peshawar Campus III Bannu, Bannu 28100, Pakistan

\* Correspondence: jiangyuhong@cug.edu.cn

**Abstract:** The use of solar energy has shown the fastest global growth of all renewable energy sources. Efforts towards careful evaluation are required to select optimal locations for the installation of photovoltaics (PV) because their effectiveness is strongly reliant on exposure to solar irradiation. Assessing the shadows cast by nearby buildings and vegetation is essential, especially at the city scale. Due to urban complexity, conventional methods using Digital Surface Models (DSM) overestimate solar irradiation in dense urban environments. To provide further insights into this dilemma, a new modeling technique was developed for integrated 3D city modeling and solar potential assessment on building roofs using light detection and ranging (LiDAR) data. The methodology used hotspot analysis to validate the workflow in both site and without-site contexts (e.g., trees that shield small buildings). Field testing was conducted, covering a total area of 4975 square miles and 10,489 existing buildings. The results demonstrate a considerable impact of large, dense trees on the solar irradiation received by smaller buildings. Considering the site's context, a mean annual solar estimate of 99.97 kWh/m<sup>2</sup>/year was determined. Without considering the site context, this value increased by 9.3% (as a percentage of total rooftops) to 109.17 kWh/m<sup>2</sup>/year, with a peak in July and troughs in December and January. The study suggests that both factors have a substantial impact on solar potential estimations, emphasizing the importance of carefully considering the shadowing effect during PV panel installation. The research findings reveal that 1517 buildings in the downtown area of Austin have high estimated radiation ranging from 4.7 to 6.9 kWh/m<sup>2</sup>/day, providing valuable insights for the identification of optimal locations highly suitable for PV installation. Additionally, this methodology can be generalized to other cities, addressing the broader demand for renewable energy solutions.

**Keywords:** LiDAR point cloud; 3D city modeling; urban environment; smart cities



**Citation:** Waqas, H.; Jiang, Y.; Shang, J.; Munir, I.; Khan, F.U. An Integrated Approach for 3D Solar Potential Assessment at the City Scale. *Remote Sens.* **2023**, *15*, 5616. <https://doi.org/10.3390/rs15235616>

Academic Editors: Filiberto Chiabrando and Jorge Delgado García

Received: 18 October 2023

Revised: 17 November 2023

Accepted: 28 November 2023

Published: 3 December 2023



**Copyright:** © 2023 by the authors. Licensee MDPI, Basel, Switzerland. This article is an open access article distributed under the terms and conditions of the Creative Commons Attribution (CC BY) license (<https://creativecommons.org/licenses/by/4.0/>).

## 1. Introduction

The European Union (EU) has prioritized the integration of renewable energy sources, with solar energy being a particularly promising option due to recent remarkable developments [1,2]. Addressing climate change requires a transition from conventional energy sources to sustainable renewables, particularly solar PV. As a result of increased awareness and competition, rooftop solar PV, which is currently underutilized, is essential to this transition [3]. Urban rooftop PV installations have gained considerable attention, especially for their potential to replace fossil fuels, offering a sustainable solution to meet the electricity need [4]. The burning of larger quantities of fossil fuels for electricity generation leads to a rise in carbon emissions, which in turn contributes to the warming of the atmosphere

and ultimately leads to climate change [5]. Utilizing solar power from rooftops can help to decrease our dependence on fossil fuels. Urban rooftops offer significant potential for PV installation, despite the complexities of urban environments [6]. As more consumers select rooftops for PV installation, companies require data and tools to predict solar irradiation [7]. However, accurately predicting solar irradiation becomes crucial with the growing use of rooftop PV installations [8]. By 2030, building-integrated PV in EU member states is projected to surpass 22% of Europe's annual power consumption [1,9].

Renewable energy is essential for the development of smart cities [10], with solar irradiation being an easily accessible and efficient source for electricity, water heating, and more [11]. Urban areas face higher energy consumption rates than rural areas due to their larger populations [12]. Many cities worldwide have established their own solar maps for PV installations [13–15]. The United States (US) shows significant interest in solar energy investment for future energy requirements [16]. While selecting appropriate rooftops for PV installations is important, the lack of reliable site context data poses challenges [6]. Urban areas feature diverse building structures, heights, and surrounding vegetation, including tall trees that cast significant shadows on rooftops. Therefore, a comprehensive understanding of the aforementioned points is essential for the precise estimation of the solar irradiation potential and informed decisions about solar PV installation [17,18]. In urban environments, direct incoming solar irradiation on small buildings is notably decreased due to the obstruction caused by larger buildings. Additionally, 3D solar irradiation modeling assessments have various limitations, leading to insufficient constraints and inaccurate estimations of solar irradiation for buildings. Consequently, this can result in misinterpretations of their energy demands [19].

To date, only a few studies have been conducted on 3D solar irradiation estimation (SIE) using a raster Digital Surface Model (DSM) at the city scale [19–22]. These studies [23,24] found yearly solar irradiation losses due to vegetation, but this is a time-consuming method for large areas. Moreover, these studies did not consider the effects of the site context and large vegetation on SIE, a key gap that this study aims to elucidate. In a previous research study, photogrammetry data were used to determine the influence of the site context on the total solar irradiation in the architectural environment on a small scale [25]. Another study illustrated how the site context affected solar irradiation [26]. The study by [27] focused on the city of Lethbridge, utilizing a multi-criteria approach that incorporated GIS and LiDAR to assess the potential for rooftop photovoltaic electricity. The study highlighted the importance of making informed policy decisions regarding investments in renewable energy within the local context. Our findings have a broader scope than merely one city (Austin is used as an example), seeking to demonstrate how the methodology can be applied to other cities. This highlights its potential to meet the global demand for renewable energy solutions. Some methods ignore the influence of shadowing from urban factors in the 3D contextual environment, such as surrounding buildings and trees, and there is a lack of difference across roof segment orientations and slopes [28].

However, due to spatial limitations in the architectural environment (e.g., geodetic coordinate systems, 3D geodata in GIS web) [29,30], the data cannot be seamlessly transferred to a 3D online application, hindering city and community engagement in solar planning, a key aspect examined in this study. The approach taken in this study involves adopting a per-building strategy to present the data, which differs from previous techniques that often rely on generating raster maps covering the entire study region, a prerequisite for 3D city asset information modeling. The utilization of a LiDAR dataset is widely regarded as the optimal choice for the purpose of 3D city modeling [31,32]. Thanks to digital technology, particularly 3D technology, solar potential has experienced remarkable improvements [33,34].

An effective approach to determining how much solar radiation hits a building is to use a 3D model of the building and its surroundings that is created in CityGML format and at different levels of detail (LOD) according to the OGC CityGML standard, ranging from LOD1 to LOD4 [35]. The urban city model has the flexibility to be stored in various

compatible 3D GIS formats, such as CityGML, KML, or CityJSON [36]. In the city of Karlsruhe, Germany, the CityGML model is employed to calculate solar irradiation for 13,000 buildings [37].

The presence of tall urban trees and buildings casts shadows on small buildings, leading to a reduction in their direct light exposure [33]. A research study revealed a significant influence of the tree canopy on the estimation of street-level solar irradiation, in which the method could not fully capture the complex interactions of shadows cast by various urban elements such as trees and buildings [38–40]. Recently, studies [41–43] have suggested a method for the estimation of the potential annual energy production of PV systems on selected roofs in the regions of Skopje, the capital of North Macedonia, and Georgetown, the capital of Penang, respectively. The cited studies omitted the site-specific impact on solar estimations and lacked a validation process to assess the accuracy of their results.

Accurate 3D city and roof shapes are needed to inform solar energy options and aid non-technical users and the public in understanding the practicality of solar maps. While past research has predominantly concentrated on 2D solar maps or solar estimation in a static architectural environment (e.g., images, PDF, Excel) [44,45], often presenting data in the form of infographic photos, screenshots, Excel tables, graphs, etc., the interoperability of 3D GIS data becomes essential [35].

This research aimed to (i) evaluate how the site context influences global solar irradiation (GSI) in a 3D contextual environment, both with and without the site context in an urban environment, and validate the workflow using hotspot analysis to assess how the site context affects GSI through the integration of 3D volumetric trees (a workflow that has not been validated in the existing literature); (ii) generate 3D multipatch features and integrate solar irradiation data with 3D buildings into 3D GIS web-based applications. This approach involves combining semantic cadastral data with a 3D city model for web visualization, creating a dynamic 3D web app linked to ArcGIS Online, and exploring future possibilities in 3D web applications for Industry 4.0.

Cities globally stand to gain valuable insights from this study, which explores the impact of site surroundings, including urban vegetation and sun radiation. The data produced through this research hold significance for city planners engaged in solar project planning, conducting feasibility studies, and developing 3D web-based applications.

## 2. Methodology

### 2.1. Case Study

Texas, in the United States of America, has relied heavily on fossil fuels such as natural gas and coal to meet its energy demands [46]. When fossil fuels are burned, a large quantity of carbon dioxide is released [47]. Carbon emissions, which trap heat in the atmosphere, induce micro to macro climate change [48]. SIE is a more sustainable approach to reducing the use of fossil fuels [49]. More efficient solar energy utilization reduces the dependence on fossil fuels for energy generation in urban environments. The suggested method is used in the study area, which is situated in the downtown capital city of Austin, Texas. The area has high-rise buildings ranging in height from 10 to 690 feet. The location map of Austin, Texas, is shown in Figure 1.

For 3D SIE to provide the best results, accurate modeling of the site context at the city scale is necessary. However, 3D city models are often challenging to obtain due to variations between the images, tools, and software used to extract the models, a difficulty described in this study. The study used LiDAR point cloud (PC) data to create a surface model and generate 3D buildings and trees. The results provided rooftop solar irradiation potential estimations. In city-scale solar project planning, the data, which include both geometric and semantic information, play a vital role.

Figure 2 shows the proposed methodology for this study.

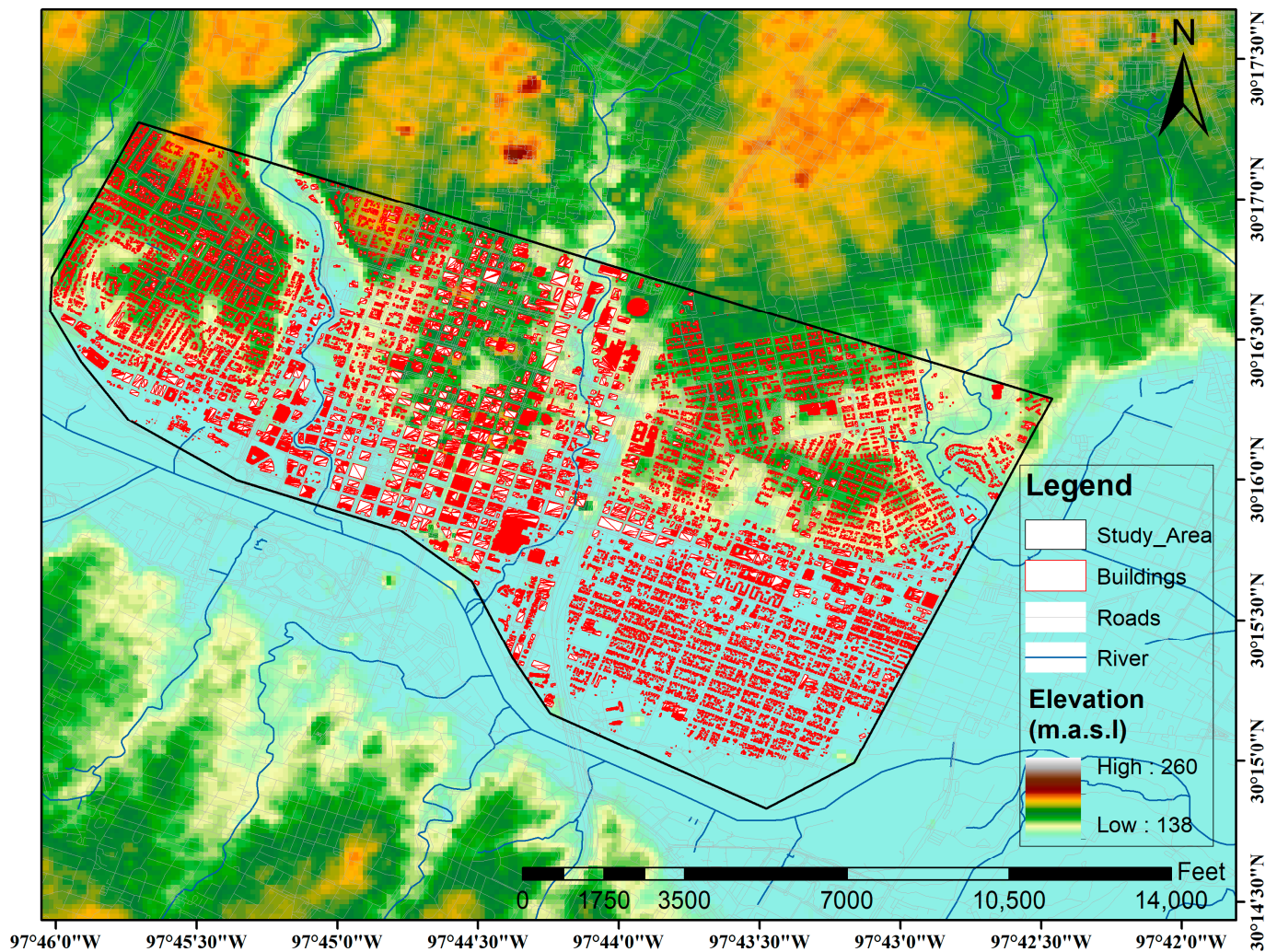


**Figure 1.** Location map of the study area.

## 2.2. LiDAR Dataset

The Texas Natural Resources Information System (TNRIS) is a Texas government agency that provides a costly data library, including free LiDAR data, that can be downloaded by quadrangles after searching for an area of interest (see link in Table 1). The files were downloaded as a zip file, containing 12 tiles of the LiDAR point cloud. Along with the LiDAR point cloud, the other files were downloaded, which contained LiDAR acquisition specification reports and valuable information (Table 1). The city of Austin Open Data Portal (AODP) hosts various geospatial and non-spatial data, which can be easily downloaded via the link (Table 1).

**Table 1.** Details of actual LiDAR acquisition.

Attribute	Value
Source	<a href="https://data.tnris.org/?pg=1&amp;inc=24#5.5/31.33/-99.341">https://data.tnris.org/?pg=1&amp;inc=24#5.5/31.33/-99.341</a> (accessed on 23 November 2021)
Dataset Name	LiDAR Austin East/West/SW-2017 50 cm-central-Texas
Derived Maps	Aerial imaging, cadastral, and land parcel
Collection Timeframe	28 January 2017 through 22 March 2017
Spatial Reference	Transverse Mercator (UTM) Zone 14N

Table 1. Cont.

Attribute	Value
Classified pointcloud with Class Codes	1 = unclassified, 2 = bare earth ground, 3 = low vegetation, 4 = medium vegetation, 5 = high vegetation, 6 = buildings, 7 = low point/noise, 9 = water, 10 = ignored ground ((1 × NPS) near BL), 13 = bridges, 14 = culverts
Collection Area	5804 sq mi
Linear Unit	meter
Flight Lines	457 (434 flight lines, 16 cross-ties, and 7 filler lines)
Vertical Spatial Reference	North American Vertical Datum 1988 (NAVD88), Geoid 12b
Sensor Type	Riegl R680i
Camera Serial Numbers	Unit 165, 863, 216
Vertical Accuracy (NVA Checkpoints)	RMSE 5.35, 95% Percentile 11.248 cm
Vegetated Vertical Accuracy (VVA)	RMSE 5.496, 95% Percentile 10.700 cm
Nominal Post Spacing (NPS)	0.50 m
Scan Angle	60 degrees
Average Ground Speed	127 Knts (flight speed)
Laser Pulse Rate	330 kHz
Scan Rate	130 Hz
Average Flying Altitude	2869 ft above mean terrain (AMT)
Aggregated Nominal Point Spacing (ANPS)	0.48 m
Aggregated Nominal Point Density (ANPD)	4.39 pts/m <sup>2</sup>

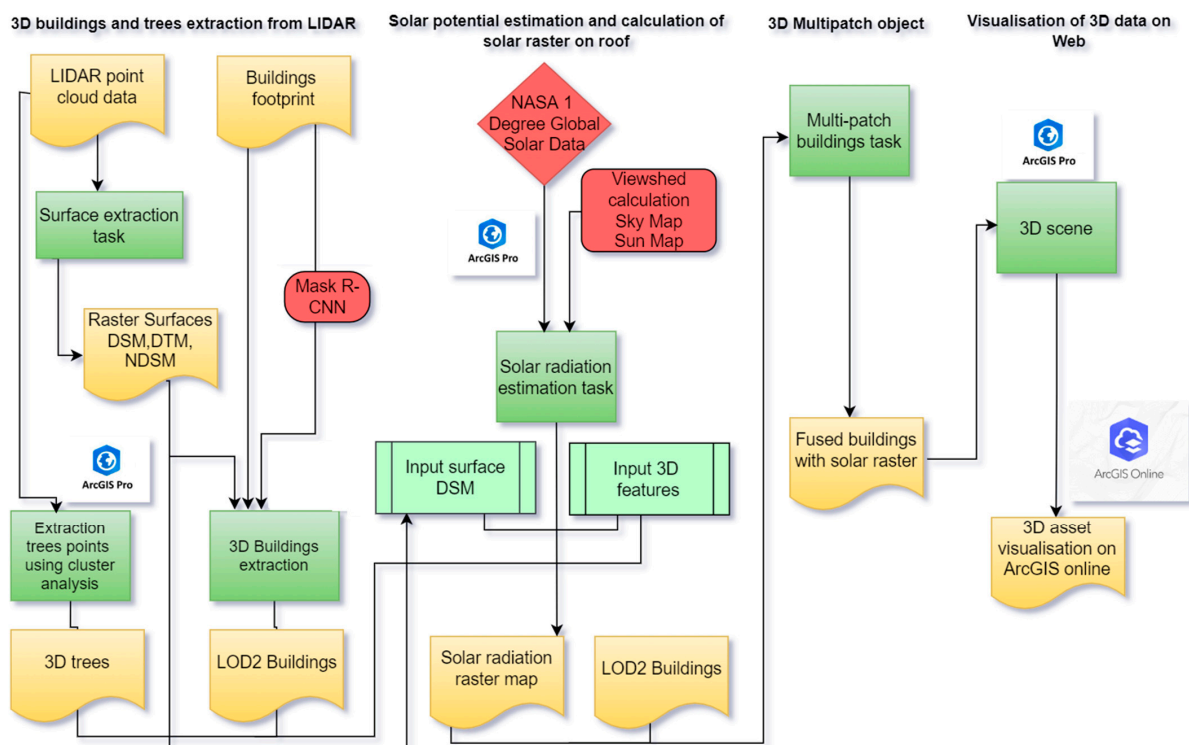


Figure 2. Overview of the developed methodology.

### 2.2.1. 3D City Model

A 3D city model is a three-dimensional digital representation of a city. A 3D city model serves as the foundation for the estimation of 3D solar irradiation. The model can be reconstructed from GIS data such as aerial photographs, point clouds, 2D building footprints, and other supplementary data, such as CAD data and remote sensing methods. Unlike 2D building footprint data, which can be found in any GIS or CAD format, 3D building footprint data store building height information along with other semantic details in their attributes. Using building footprints as LOD0, CityGML 2.0 employs the LOD concept to identify multi-scale representations of semantic 3D city models [50]. One of the most important characteristics of a 3D city model is its LOD, which relates to the model's resemblance to its real-world equivalent and has implications for usability. According to CityGML 2.0, it has been divided into five categories based on thematic appearance and geometric/semantic complexity [51]. LOD0 can be used to create LOD1 levels of buildings by extruding the building shape based on height information [52]. LOD1 represents a 3D volumetric representation of the building but does not represent any roof shapes, such as flat, gable, or hip, which are important for SIE. To represent the real 3D building shape up to LOD2, 3D point cloud data are widely used to extract the highest LOD. For the scope of this research study, the LOD was kept up to LOD2.

### 2.2.2. LOD2 Building Extraction

LiDAR data are increasingly being used for such purposes since they offer topological and geographic information. Laser light is sent from the sensor on the drone towards the Earth's surface, which reflects back from the objects, and the sensor receives the reflected light and records it. LiDAR can measure distance, which can be converted into height, and it can differentiate trees from other objects. In the LAS format version 1.4, the point cloud data were categorized based on the American Society for Photogrammetry and Remote Sensing (ASPRS) classification rules. The classified point cloud was used to extract 3D surfaces, including the digital terrain model and digital surface model (DTM and DSM), and the difference between the DTM and DSM normalized digital surface model (NDSM), to compute the absolute height information of any feature on the ground. The DTM represents the ground features, such as terrain, while the DSM represents any feature above the ground (for details, see Tu Delft GEO1015.2021) [53].

The accuracy of 3D building extraction in such studies often relies on the resolution of DSMs. To achieve this, LiDAR data with a fixed cell size of 1.5 feet were employed. However, a notable challenge emerged during the building object detection process, wherein variations in building roof height and shape led to instances where one building encompassed multiple roofs of different heights, as illustrated in Figure 3a. A single image was taken to provide a clearer understanding. Figure 3b illustrates that the general process of 3D building extraction, when using the built-in 3D BaseMap solution package in ArcGIS Pro 3.2, does not consider this information. This limitation was addressed by leveraging the deep learning (DL) model Mask R-CNN. Transfer learning was used in order to enhance the results without the need for huge quantities of training data and intensive hyperparameter tuning [54]. The approach employed in this study involved the utilization of a pre-trained Mask-RCNN, which had been previously trained on a dataset relevant to the research topic (referred to as the source dataset) [55]. The image processing steps were performed, such as image transforms, enhancement, and data augmentation, which improved the image quality considerably, making them more suited for analysis [56]. To enhance the effectiveness of feature extraction in building footprint identification through image segmentation, careful efforts were made to accurately extract and categorize the buildings from the 2D raster [57]. We applied random transformations like scaling images by up to twenty percent and occasionally flipping them horizontally. Along with the original images, this process led to improved images [58]. Subsequently, the model was partly retrained using our specific target dataset. The pre-trained Mask R-CNN model was employed, and fine-tuning was performed on images. This process aimed to enhance the accuracy of feature extraction

through instance segmentation and the detection of objects. The primary focus was on identifying accurate building footprints within 2D images [58]. As shown in Figure 3b, building footprint extraction represents the general process where a single building structure is delineated and identified. While the segmented footprint contains three new feature classes using Mask R-CNN (Figure 3c), the resulting 3D structure provides an accurate representation of the buildings (Figure 3d). The segmented building footprints were ultimately saved in a geodatabase file within the package directory. Figure 3d illustrates the final 3D buildings, which were created by assigning heights based on the derived DTM. This process resulted in a 3D BaseMap solution specifically representing buildings at LOD2.

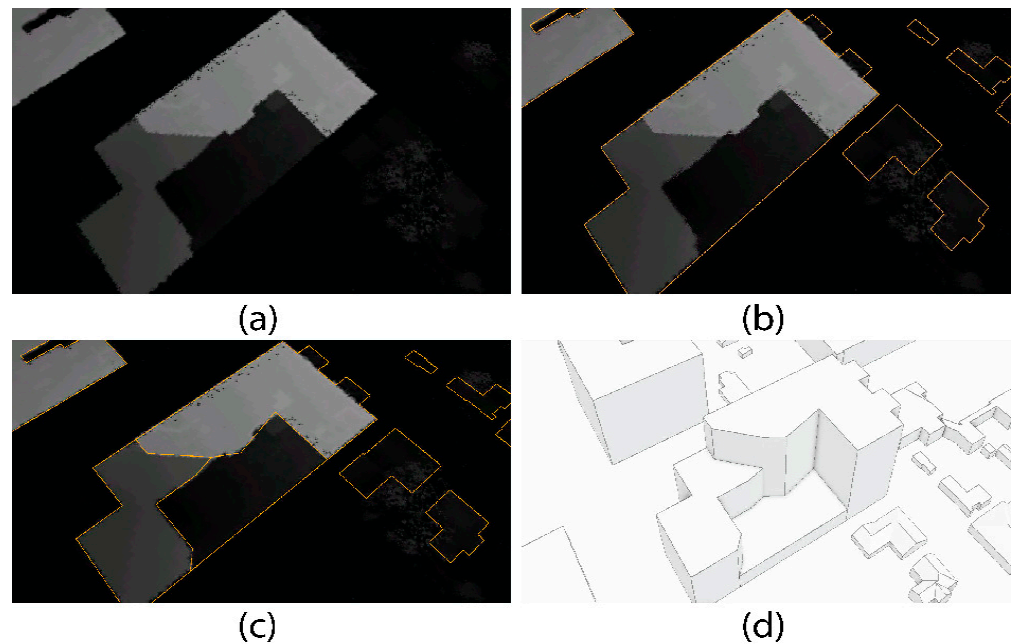


**Figure 3.** (a) Raster DSM having three different building segments. (b) General 3D building extraction process in ArcGIS Pro 3.2 (As indicated by the yellow shading building footprint have one segment). (c) Building footprint segmentation using Mask R-CNN (As indicated by the yellow shading building footprints have three segments). (d) Final 3D building representation in LOD2.

### 2.2.3. 3D Tree Extraction

Furthermore, unlike 3D buildings, extracting trees from LiDAR data is challenging due to the absence of an accurate predefined boundary. The existing 3D BaseMaps solution provided several tree extraction options based on the input data. However, in our study, the 3D tree points were extracted using density-based spatial clustering algorithms [59]. Clustering is a method of simplifying the symbology of a complex layer of points. A cluster is used to represent two or more point features. Feature clustering is the process of grouping individual point features together into clusters. The algorithm used in this process utilizes data from the vegetation class of LiDAR data. Using these parameters, the algorithm is able to extract 3D tree points and establish minimum bounding geometry. The result of this procedure is a collection of 3D tree points that contain important data, such as tree height and width. This information is then used in the creation of 3D procedural tree models. Figure 4a–c show the overall overview of 3D procedural tree modeling.

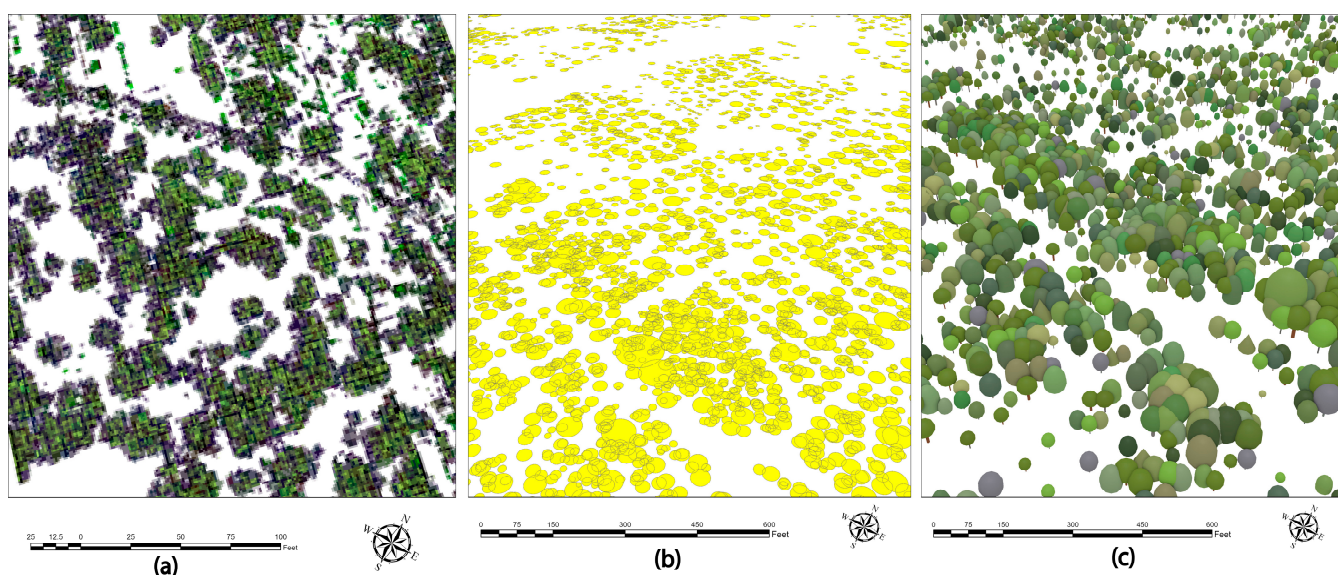


**Figure 4.** LiDAR vegetation class, vector to 3D volumetric trees, (a) LiDAR point cloud class, (b) 3D trees point and minimum bounding geometry, (c) 3D volumetric trees.

### 2.3. Solar Irradiation Model

Urban buildings have a high solar irradiation capacity, making the installation of solar panels for different purposes cost-effective and ecologically friendly. Urban environments include complex topologies, diverse building designs and heights, and vegetation, which can impact solar irradiation. Estimating solar irradiation for multiple buildings at the city scale demands high-performance software and hardware [60]. Built-in GIS tools assess solar irradiation in seconds, making them useful for the estimation of the solar PV potential in urban areas. Various solar irradiation models, predominantly dependent on geographical and atmospheric parameters, consider the specific geographical location of the area [61,62]. However, many of these models assume uniform solar irradiation for every point on a building's surface, leading to inaccuracies in the results. They often overlook factors like the surface slope or the impact of shadows, such as those cast by trees, which can have a significant influence on the results.

The ESRI-based Solar Analyst tool developed by Fu et al. [63] uses a viewshed algorithm. This tool does not inherently model clouds, as clouds are very complex to predict or model. This modeling tool was tested and validated by comparing estimated temporal and spatial insolation (solar irradiation) patterns in the region of the Rocky Mountain Biological Laboratory (RMBL) with detailed weather, vegetation, and monitoring of insolation (solar irradiation). Recently, several studies at the urban scale have also used and validated this modeling tool [25,64,65]. Generally, the implementation of this approach is a challenging task. While it does not inherently model clouds due to their complexity, it considers shadows from surrounding buildings and trees, allowing for modeling over inclined surfaces, which is particularly useful in urban landscapes. The tool can integrate attributes that vary spatially over large regions, making its implementation a challenging yet powerful process. The basic principle behind this modeling tool is a four-step process: (i) viewshed calculation; (ii) sunmap calculation; (iii) skymap calculation; and (iv) overlay of viewsheds with sunmaps and skymaps.

The viewshed is a raster representation of the entire sky that is visible or obstructed when viewed from a particular location on the Earth. This is similar to the view provided by the upward-looking hemispherical fisheye photograph [66]. The skymap and sunmap were overlaid on the viewshed, as shown in Figure 5. The gap fraction is the proportion of unobstructed sky area in each skymap or sunmap sector, which is calculated by dividing the number of unobstructed cells by the total number of cells in that sector. The total global irradiation is the sum of direct and diffuse solar irradiation, where  $Global_{tot} = Dir_{tot} + Dif_{tot}$ .

where  $Dir_{tot}$  represents the direct solar irradiation. It is determined on the surface from the sunmap with a solar constant of  $1367 \text{ W/m}^2$  (the value recommended by the World Meteorological Organization (WMO)) and the calculation of the zenith angle. Meanwhile, for  $Dif_{tot}$ , diffusive radiation was calculated using either the uniform sky or standard overcast models [67].

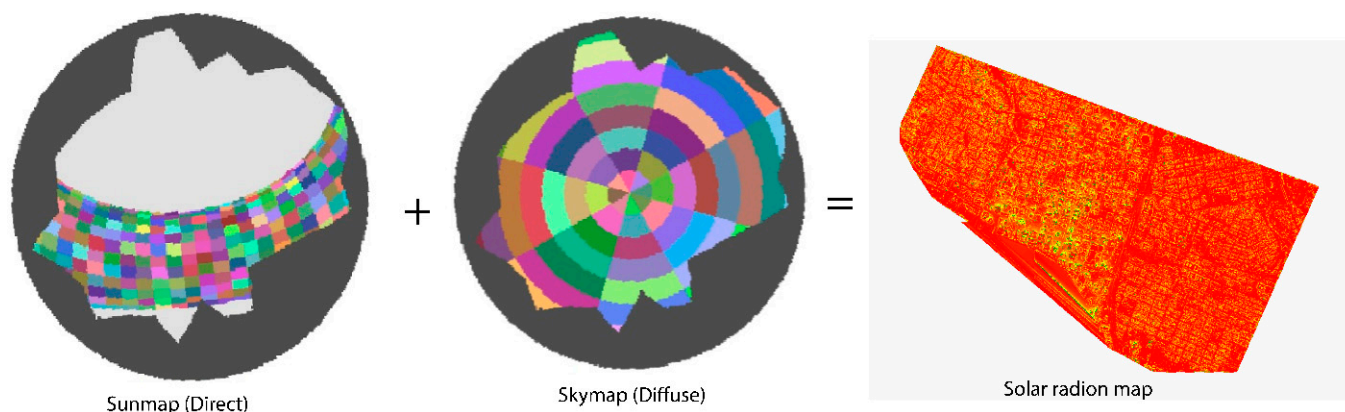


Figure 5. Viewshed analysis to solar raster map.

Within this study, we utilized an established ArcGIS Pro 3.2 solar irradiation model employing the viewshed algorithm to compute the total global radiation on a monthly and yearly basis. The model requires a 2.5-dimensional surface that serves as input, alongside a 3D site information model containing buildings and trees. Preceding the 3D city model process, 3D multipatch building objects were generated, providing essential inputs for subsequent analyses. Two solar irradiation models were developed in line with the study scope:

- I. without site context (A);
- II. with site context (B).

Figure 6a, demonstrates the site context model using only the DSM (without built surroundings) as an input file. In contrast, Figure 6b includes the built environment, incorporating trees and buildings.

In areas with dense vegetation and tall trees, solar panel points on rooftops were spaced at  $1.5 \text{ ft} \times 1.5 \text{ ft}$  intervals. The resulting annual average SIE map was divided into zones, as shown in Figure 6c, with dark red buildings receiving more solar irradiation, followed by light orange to dark orange buildings.

#### 2.4. Evaluating Solar Irradiation with 3D City Model

The present study employed a four-step methodology to analyze solar irradiation. This methodology encompassed the calculation of viewsheds, sunmaps, skymaps, and the subsequent overlay of viewsheds with sunmaps and skymaps. The methodology utilized LOD2 buildings and high vegetation, in conjunction with the DSM, for the purpose of analysis. The solar data obtained from NASA's 1-Degree Global Dataset were employed, and the analysis was conducted using the standard overcast sky model; see [power.larc.nasa.gov](https://power.larc.nasa.gov) [68] for more details. The solar irradiation task utilized default parameters, including a sky size of 200, a zenith division of 8, and an azimuth division of 8. The sky dome was divided into 8 parts each for both vertical and horizontal angles, facilitating a thorough depiction of the sun's motion and location throughout the day and year. By employing 8 divisions in both the vertical and horizontal orientations, the solar irradiation analysis generated comprehensive sun position data at consistent intervals. The level of resolution employed in this study enabled a better representation of solar shadows, direct sunlight, and the distribution of solar energy over the study area. The calculation of solar irradiation raster maps requires significant computational resources and memory capacity. To optimize the efficiency, the cell size was maintained at  $1.5 \text{ ft} \times 1.5 \text{ ft}$  for the resultant solar irradiation

raster. Analysis with  $1.5 \text{ ft} \times 1.5 \text{ ft}$  was deemed suitable for the scope of this research. For PV installation planning, a larger cell size is advised to better measure radiation differentials. The approach performed well because the overall results remained unaffected by the cell size for the larger area. The output solar raster maps were categorized on a monthly and yearly basis, with quantification measured in  $\text{kWh}/\text{m}^2\text{-year}$ .

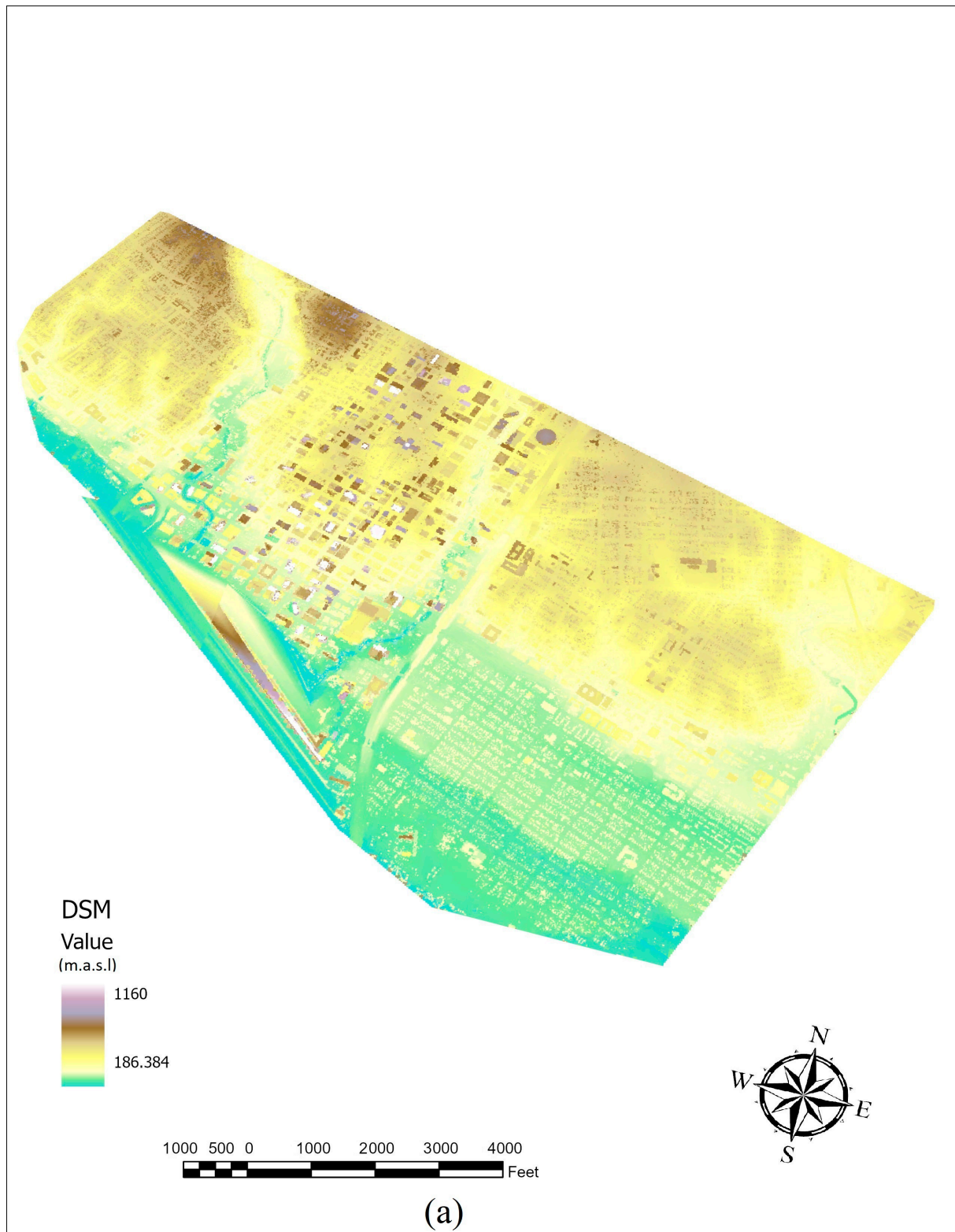


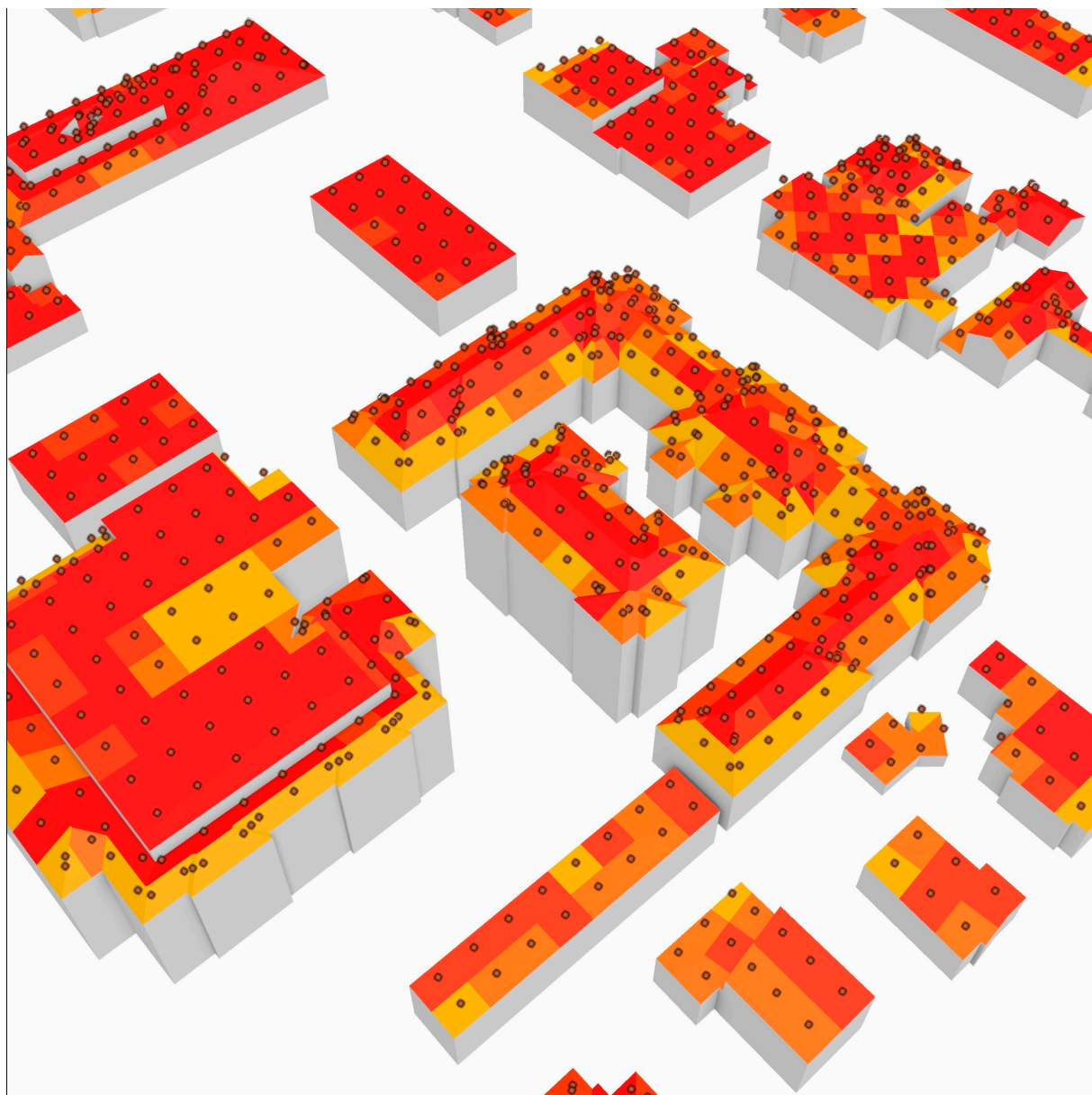
Figure 6. Cont.



(b)



Figure 6. Cont.



### Legend

● Solar Roof Panel Points

Radiation\_kWh/m<sup>2</sup>-year

0.000000

Low > - 2.44

Medium > - 3.46

High > - 5.58

Very High > - 6.36

56 28 0 56 112 168 224 Feet



(c)

**Figure 6.** (a) A site without context Digital Surface Model, (b) B with site context LOD2 buildings and 3D volumetric trees, (c) high-resolution solar raster mapping on rooftops with solar panels.

The approach employed in this study utilized the OGC CityGML standard as a means to construct a 3D city model, thereby facilitating a thorough digital representation of the urban area in three spatial dimensions. The LOD2 level encompassed the representation of buildings and trees, providing comprehensive data regarding their structure and height.

By draping all vertical characteristics over the DTM, we achieved seamless integration and a realistic 3D city model.

### 3. Analysis and Results

#### 3.1. Annual Solar Irradiation Potential Estimation

The research area was analyzed to determine the average annual GSI in 2022. Figures 7 and 8 show the scenarios with site and without site context. The results revealed that the highest average solar irradiation for the entire year, reaching 7.00 kWh/m<sup>2</sup>, was observed using a 1.5 ft × 1.5 ft grid size on building roofs. During July, the peak solar irradiation on the roof was recorded as 5.6 kWh/m<sup>2</sup> with site context and 6.9 kWh/m<sup>2</sup> without site context. In contrast, the lowest values were observed in December, with solar irradiation reaching 2.8 kWh/m<sup>2</sup> with site context and up to 3.0 kWh/m<sup>2</sup> without site context. These findings are in line with the outcomes of previous research studies conducted by Zhang, et al. [21] and Teyabeen, et al. [69], corroborating the accuracy and reliability of our analysis. Moreover, the site context model played a crucial role in revealing the impact of the high tree density on the southeast side of the study area. It indicated that solar irradiation was significantly reduced due to the presence of dense vegetation in that particular region. The site context model was proven to understand the spatial distribution of solar irradiation across the research area and provide insights into how various environmental factors, such as tree density, can influence solar energy availability. A more detailed analysis of the spatial distribution of solar irradiation across the research area can be found in the site impact analysis.

Figure 9 illustrates the comparison of the number of buildings (*y*-axis) with solar irradiation values (*x*-axis), emphasizing the significant differences between the ‘with context’ and ‘without context’ scenarios. As an example, in the scenario where context is not considered, there are 1517 buildings with solar irradiation values ranging from 4.7 to 4.9 kWh/m<sup>2</sup>. However, when the context is taken into account, this corresponds to a reduction of approximately 45%, to 825 buildings. The decrease in building count can be attributed to the presence of trees, as the site context considers their impact on the estimates. Conversely, when the site context is not considered, the number of buildings automatically increases. Figure 9 effectively demonstrates that the site context significantly influences the estimates of total solar irradiation (i.e., certain numbers of buildings). It highlights that when the site context is considered, the number of buildings decreases, indicating a notable impact on SIE. The phenomenon is further illustrated by showcasing a large number of small buildings that are most affected in the study area.

Furthermore, Figures 7 and 8 illustrate the results of the whole year SIE with site and without site context. The analysis considered a total of 10,490 buildings, calculating the total amount of solar irradiation that each roof received in kWh/m<sup>2</sup>/year. The results reveal that the SIE values are 99.97 kWh/m<sup>2</sup> with context and 109.17 kWh/m<sup>2</sup> without site context (as a percentage of the total roofs). This represents a decrease of approximately 9.3% when the context is considered.

Moreover, Figures 7 and 8 reveal that the randomly selected value (with a context of 3.01 kWh/m<sup>2</sup>/day, highlighted in red) is lower than the estimated value (without a site context of 4.44 kWh/m<sup>2</sup>/day). For detailed information, refer to the link provided in the Conclusions section. The findings of our study highlight the significant impact of vegetation on incoming solar energy.



Figure 7. Whole year solar irradiation estimation with site context.

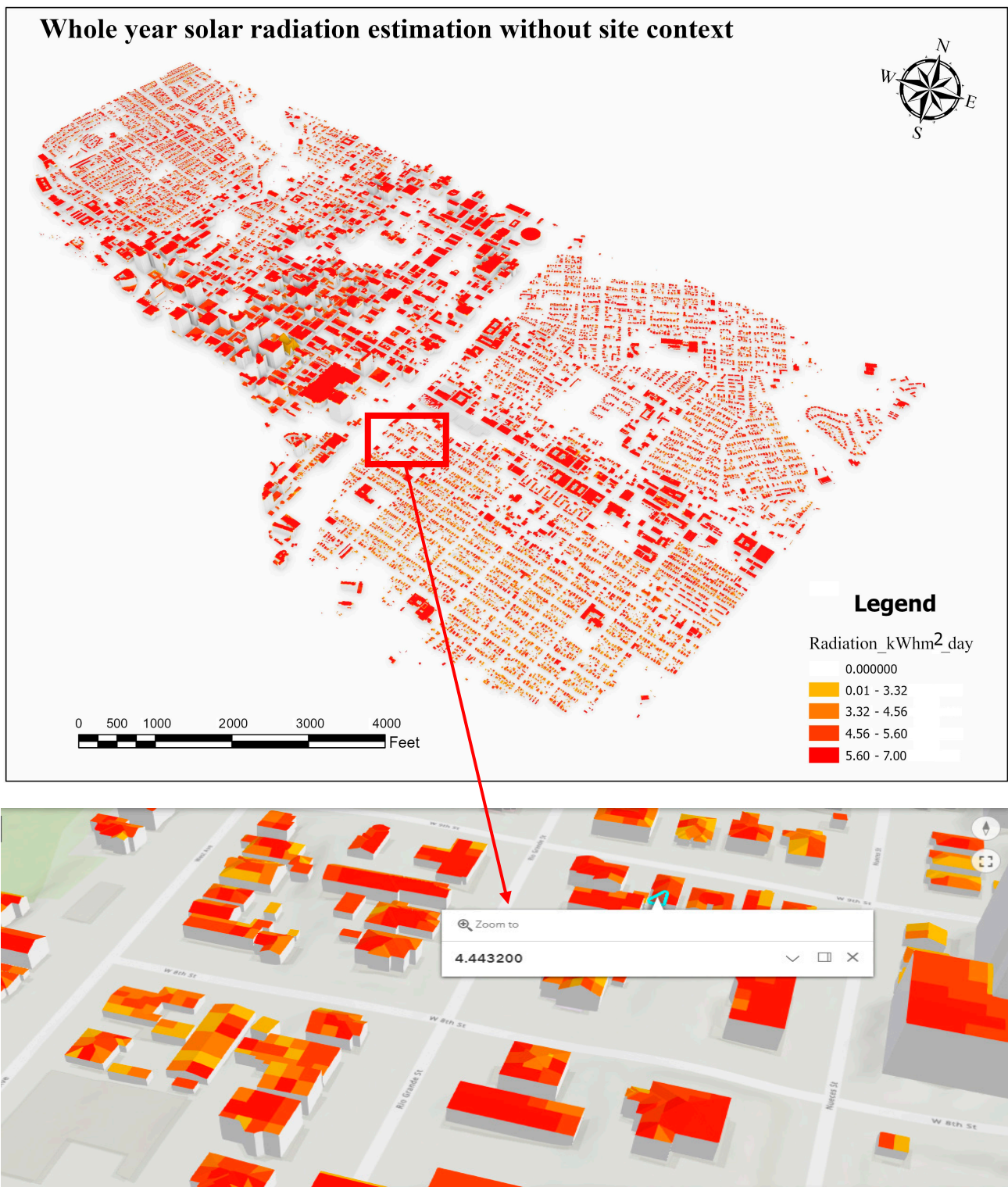
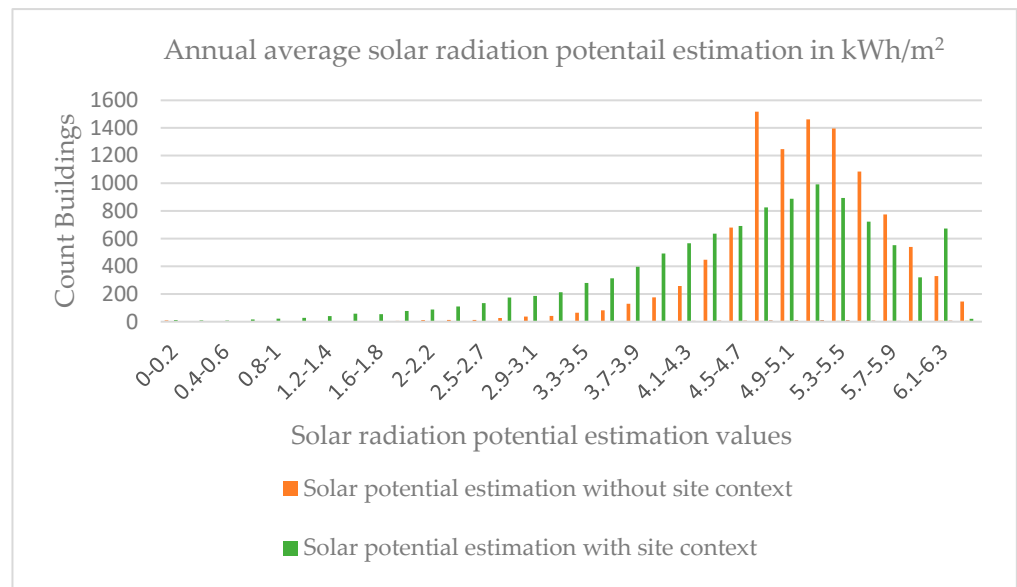


Figure 8. Whole year solar irradiation estimation without site context.



**Figure 9.** Annual solar irradiation estimation with site and without site context.

### 3.2. Validation

To assess the influence of the site on the GSI results from the previous step, the ArcGIS Pro 3.2 statistical tool hotspot analysis (Getis-Ord  $G_i^*$ ) from the Spatial Statistics toolset was used to find spatial autocorrelation patterns for each feature in the dataset. This was done by identifying the differences between features that were clustered (hotspots) and features that were spread out (coldspots). This statistical method facilitated the identification of areas with statistically significant high or low values in comparison to their neighboring features. According to Kowe et al. [70], hotspot analysis is considered the best method for the analysis of large geospatial data, and it is used for the first time in this study. The extracted 3D tree point feature class was employed to locate the hotspots, containing valuable information such as tree height, width, and other auxiliary details retrieved from LiDAR data. The hotspot analysis tool in ArcGIS Pro 3.2 identifies spatial clusters with statistically significant high or low attribute values [71]. Given a set of weighted data points, such as the number of trees where the height is spatially weighted by the width of each tree, it operates under the assumption that data values are spread randomly across the study area. This tool identifies “hotspots”, which are clusters of data points with higher tree densities than expected. The hotspot analysis also delineates spatial clusters of lower-than-expected tree density [71]. The mathematical model of Getis-Ord  $G_i^*$ , or the Getis-Ord local statistic, is given as follows:

$$G_i^* = \frac{\sum_{j=1}^n w_{i,j} x_j - \bar{X} \sum_{j=1}^n w_{i,j}}{S \sqrt{\frac{n \sum_{j=1}^n w_{i,j}^2 - (\sum_{j=1}^n w_{i,j})^2}{n-1}}} \quad (1)$$

$$\bar{X} = \frac{\sum_{j=1}^n x_j}{n} \quad (2)$$

$$S = \frac{\sum_{j=1}^n x_j^2}{n} - (\bar{X})^2 \quad (3)$$

Equation (1) represents the relationship between the attribute value  $x_j$  for feature  $j$ , the spatial weight  $w_{i,j}$  between features  $i$  and  $j$ , and the total number of features  $n$ . As the  $G_i^*$  statistic is a z-score, no additional calculations were required. Equation (2) determines the overall spatial autocorrelation of the attribute values for all features. The calculation involves finding the average of the  $G_i^*$  statistics for all features. Equation (3) computes the  $p$ -value for the overall spatial autocorrelation statistic. The  $p$ -value represents the likelihood

of obtaining a value of  $G$  or more extreme than the observed value assuming that there is no spatial autocorrelation. The input data should be a point or a magnified point for any geographic zone. However, the most significant factor that affects the output result before conducting hotspot analysis is the conceptualization of spatial relationships. There is a broad theory and best practice for the modeling of spatial relationships between features available on the ESRI website. For the sake of this study's feasibility, we opted for the fixed-distance band option to conceptualize spatial relationships. The steps in determining how a site affects solar irradiation are as follows: (i) finding hotspots and coldspots for tree points based on height and width as a weighted field; (ii) visually depicting a hotspot where dense and tall trees appear; (iii) finding the difference in average solar irradiation with and without context data; and (iv) finding the hotspot and coldspot where the difference appears in the global solar result. The return of this tool is the  $G_i^*$  statistic, which comprises a  $z$ -score and  $p$ -value for each feature in the dataset. For statistically significant positive  $z$ -scores, a larger  $z$ -score shows more intense clustering of high values (hotspot). For statistically significant negative  $z$ -scores, the smaller the  $z$ -score is, the more intense the clustering of low values (coldspot). The use of  $G_i^*$  statistics involves examining the  $z$  and  $p$ -values to interpret the hotspot analysis result.  $G_i^*$  statistics return  $z$ - and  $p$ -values, while the  $G_i^*$   $z$ -score is displayed at a 238-foot threshold distance band. A higher positive  $z$ -value and lower  $p$ -value represent the clustering of high tree data points (hotspot), indicating areas with high tree density. Conversely, a larger negative  $z$ -value and lower  $p$ -value indicate the clustering of low tree height points, representing coldspots with fewer trees and low tree density. The  $G_i$ -Bin score ranges from 0 to 3, with a positive higher value of 3 indicating a 99% confidence level of highly clustered points (hotspots with very high tree density) and a  $-3$  value indicating a coldspot of very low tree density, with 95% confidence.

At  $+2$   $G_i$ -bin, points are moderately clustered with hotspots in areas of medium–high tree density, while  $-2$   $G_i$ -bin represents a coldspot in an area of low tree density. At a 90% confidence level,  $\pm 1$   $G_i$ -bin indicates low clustering with low hotspots and lower high tree density at  $+1$   $G_i$ -bin and low coldspots with low high tree density at  $-1$   $G_i$ -bin.

#### Site Impact Analysis

The site impact analysis aimed to assess the vegetation effects on GSI. In Figures 10 and 11, the dark red hotspots in the southeast of the study area represent dense and tall tree areas, whereas dark blue represents areas with less dense and smaller trees. Results were calculated based on point pattern analysis, representing tree positions in the real world. Table 2 presents the results of the Getis-Ord  $G_i^*$  statistics at various confidence levels. It identifies areas with extremely high and low tree density at  $+3$   $G_i$ -Bin and  $-3$   $G_i$ -Bin for a 99% confidence level, as well as areas with moderately high and moderately low tree density at  $+2$   $G_i$ -Bin and  $-2$   $G_i$ -Bin for a 96% confidence level.

**Table 2.** Hotspot analysis with Getis-Ord  $G_i^*$  statistics summary for trees.

Confidence Level (%)	$G_i$ _Bin	Pattern	Tree Spots	Tree Density
99	3	VH clustered	hotspot	VH Tall Trees
	$-3$	VH clustered	coldspot	VL Tall Trees
95	2	M clustered	hotspot	MH Tall Trees
	$-2$	M clustered	coldspot	ML Tall Trees

Table 2. Cont.

Confidence Level (%)	Gi_Bin	Pattern	Tree Spots	Tree Density
90	1	Clustered	hotspot	H
				Tall Trees
	−1	Clustered	coldspot	L
				Tall Trees

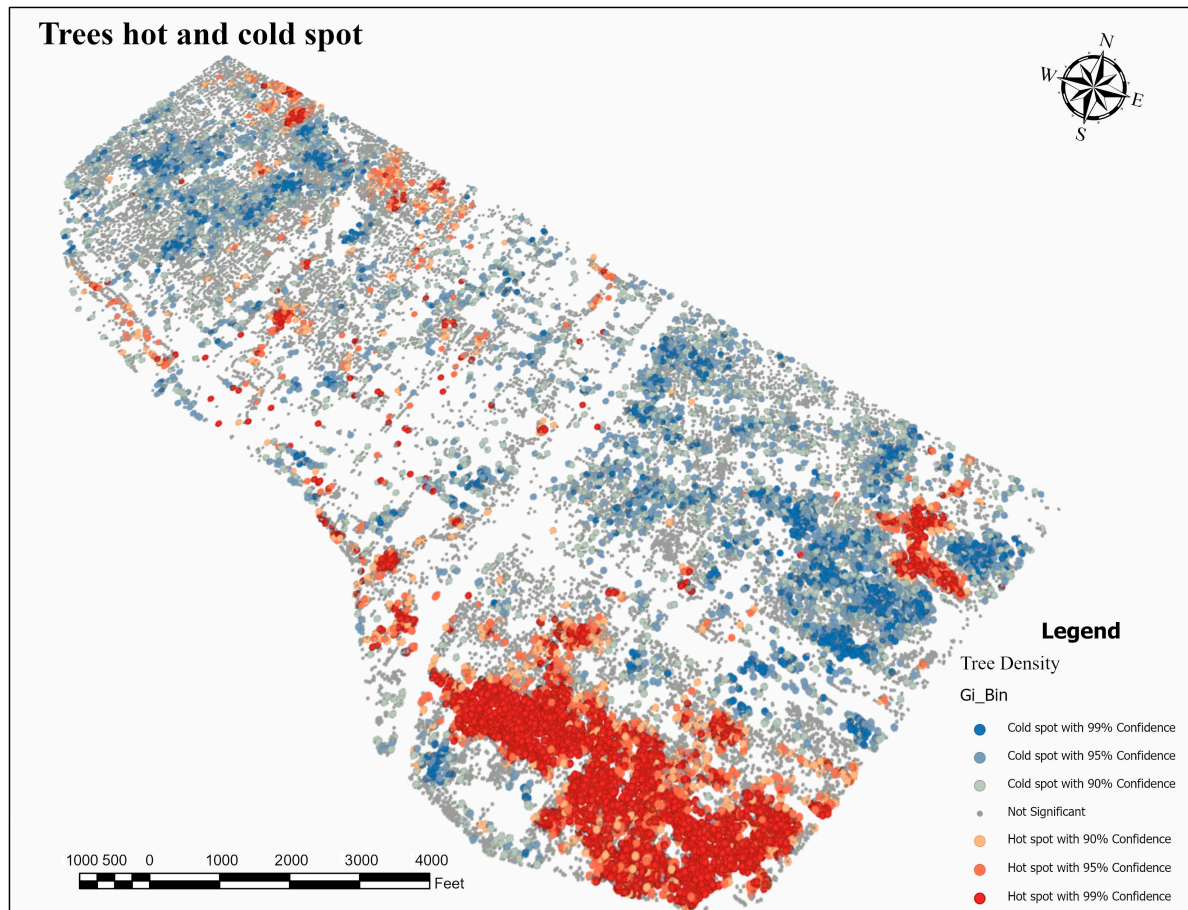
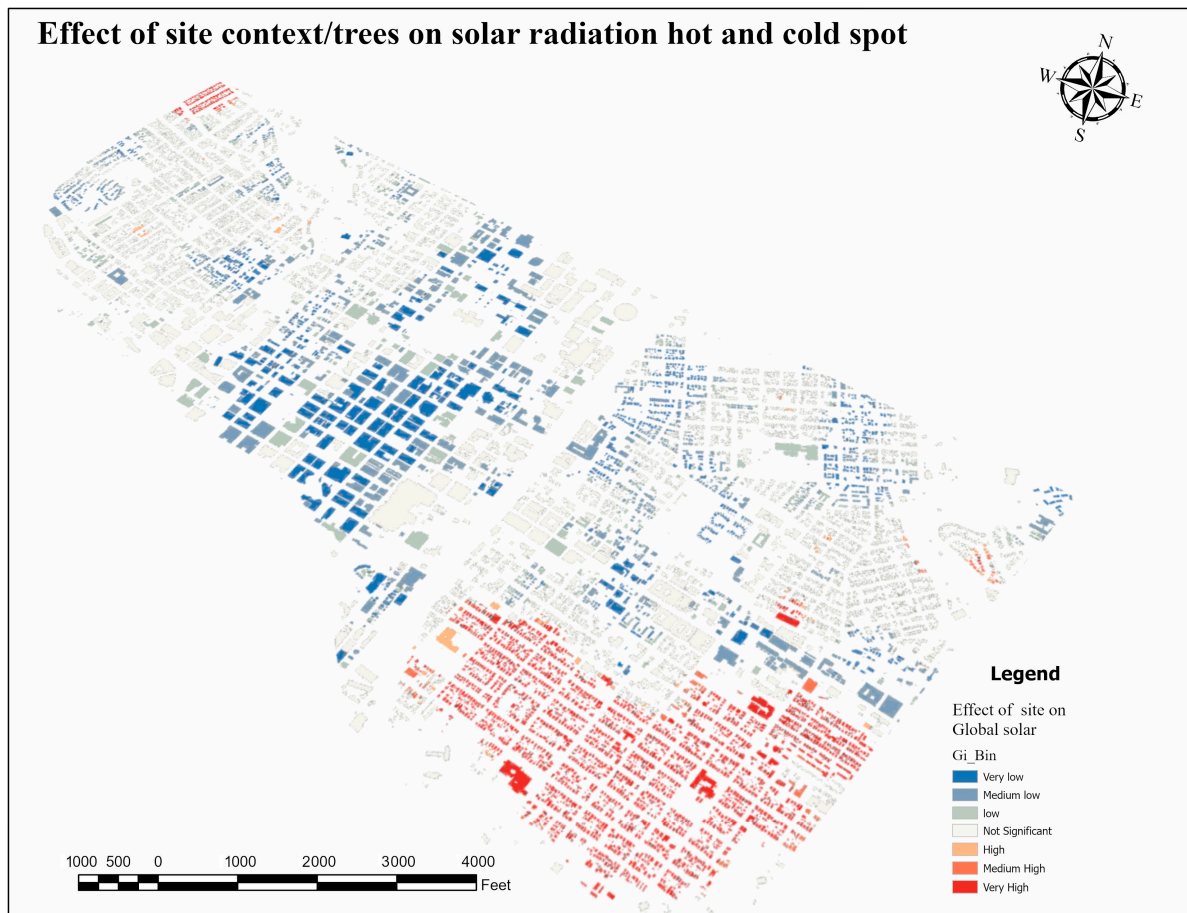


Figure 10. Tree hotspots and coldspots for the study area.

At a 90% confidence level, an increase of +1 Gi-Bin suggests areas with a higher density of tall trees, while a decrease of −1 Gi-Bin suggests areas with a lower density of tall trees.

The map shown in Figure 10 was created using tree heights weighted by tree width. The figure shows the areas with tall trees and a higher width as very high hotspots, while areas with small trees and a lower width are represented as very low coldspots.

The hotspot maps (Figures 10 and 11) were created by analyzing the difference in average solar irradiation in kWh/m<sup>2</sup>/day with and without site context. The extremely high hotspot represents an area with tall trees and a greater width, indicating a significant tree influence on solar irradiation. In contrast, the very low coldspot signifies areas with small trees and a smaller width, showing a minimal tree impact on solar irradiation.



**Figure 11.** Effect of site context/trees on GSI hotspots and coldspots.

The magnitude of the difference between solar irradiation values with and without site context determines the size of the hotspot on the map. A larger difference leads to a more extensive hotspot, while a smaller difference results in a greater coldspot. As seen in the dark blue coldspot in Figure 10, areas with little difference in solar irradiation are evident. Interestingly, the findings reveal that trees have little to no effect on areas with high-rise buildings, which is understandable given that trees are not taller than buildings and thus cannot significantly shade them. Instead, the study area experiences the most significant tree shade impact in the southeast, with a small area in the northwest also affected due to a high concentration of small residential buildings. The solar irradiation analysis highlights the critical role of selecting the most suitable location for solar panel installation (Figure 12). Areas with little variation in solar irradiation, classified as suitable (red shaded) and highly suitable (aqua shaded), emerge as prime sites for efficient energy generation. While certain areas may not be suitable (yellow shaded), exploring alternative approaches is essential. By strategically placing solar panels in suitable and highly suitable zones, along with advancements in solar technology, we can pave the way for a greener and more sustainable energy future. Embracing solar energy in these optimal locations can significantly reduce our carbon footprint and foster energy independence.

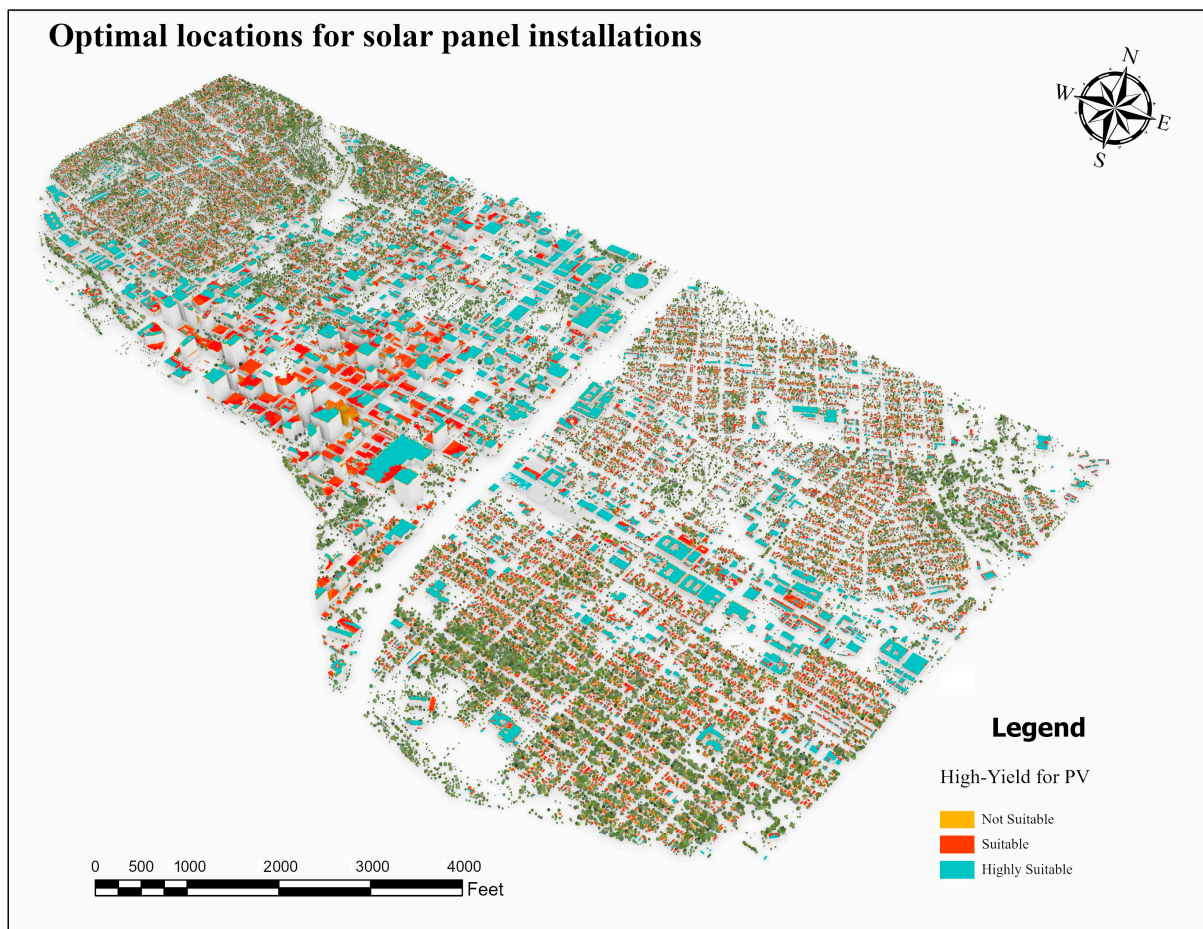


**Figure 12.** Optimal location for PV installation.

#### 4. Discussion

To estimate the solar potential in three dimensions, the study employed LiDAR data to extract 3D geometric information in accordance with OGC CityGML standards. The developed methodology was implemented in a 3184-acre study area, equivalent to 4.975 square miles, located in a section of Austin, Texas, with the aim of investigating the impact of the site context on city-scale global solar irradiation estimation.

Moreover, this research investigated the impact of the site context on city-scale global SIE. To validate the established methodology, models were utilized, both with and without site context, to identify areas with tall and dense trees. The impact of tree shadowing was mainly observed in the southeast, with a dark red hotspot, and a smaller region in the northwest, which consisted of several small residential buildings. The solar irradiation estimates, considering cases both with and without site context, revealed the highest and lowest values as 5.6 kWh/m<sup>2</sup> and 6.90 kWh/m<sup>2</sup> in July, and 2.8 kWh/m<sup>2</sup> and 3.0 kWh/m<sup>2</sup> in December, respectively, validating the accuracy of our methodology for city-scale studies. The research conducted by Teyabeen, et al. [69] supports and corroborates these findings. It is worth noting that no validated method currently exists to assess how a site's location influences GSI estimates at a city scale. This research makes a significant contribution to addressing this knowledge gap and enhancing our understanding of solar potential in urban environments. As an example, Han et al. [26] introduced a highly appropriate method for the 3D simulation of solar potential estimation in the area surrounding a small number of buildings with overestimated results. Their approach is notably more intricate than the one outlined in our study. There have been several studies on the shadow cast of urban solar potential estimation using generic models of urban layouts with a limited number of buildings, as demonstrated in the works of Brito et al. [72] and Liang et al. [60].

Moreover, some studies have investigated the effects of trees in the urban form on the solar radiation potential for new buildings in their early design phases [73]. Meanwhile, in our study, the 3D city model extraction (building's rooftop and trees) from the LiDAR point cloud based on CityGML standards (model with exchange format for representation, storage, and virtual 3D city model exchange) and solar potential estimation at a city scale was demonstrated.

In addition, the 3D building extraction process was found to be very accurate based on the visual identification of LiDAR points and the extracted 3D buildings (Figure 3: Final 3D buildings). The overall results were very promising when using the site context model. The extracted 3D building and tree results were presented as a 3D volumetric representation with semantic information. The process successfully modeled a range of roof shapes, with flat roofs being the most common, followed by gable and hip roofs. However, some of the buildings were wrongly classified during the extraction process due to their roof shapes, which had to be manually corrected. Another issue encountered was selecting data from several sources, which were acquired on various dates, resulting in the absence of some buildings, which were shown using only building LiDAR points, corrected manually.

The accuracy of a solar irradiation study is closely tied to the quality of the 3D building model used. In this study, a LiDAR dataset was employed to construct a detailed geographical and geometric model; see also Iñaki et al. [74]. The study by Li et al. [15] found that there is high uncertainty in the building extraction process. The basic assumption is made that all the areas in a single building footprint have a consistent height. However, this assumption often proves inaccurate due to the presence of varied roof shapes and heights within a single building footprint. To accurately represent the building model, this study has addressed a major challenge in building footprint height estimation based on pre-modifications of the DSM.

However, the majority of SIE studies rely on surface derivatives from classified LiDAR data, using a 2.5D urban scene as the input file; see Sredenšek et al. [75].

Our findings suggest that the northwest (central) region offers a large usable area along with sufficient solar irradiation, making it a suitable location for PV installation (Figure 12). The analysis reveals that the southwest and a small section of the southeast in downtown Austin are less suitable locations for PV installation due to their lower levels of solar irradiation. Conversely, the southeast region experiences a more pronounced tree shade impact, making it less suitable for PV installation due to reduced solar irradiation availability. However, even in these shaded areas, careful design and advanced solar technologies, such as bifacial solar panels and sun-tracking systems, offer promising options for effective solar energy harnessing. The small area in the northwest, characterized by numerous small residential buildings, necessitates careful planning to maximize solar exposure while minimizing shading from neighboring buildings.

In addition, it is important to note that existing building roofs often feature various installation elements, such as AC vents, antennas, chimneys, and overhangs, as shown in Figure 13. These elements can impact the optimal placement and efficiency of solar panels on the rooftops. They can occupy significant portions of the roof, making them unsuitable for solar panel installation, a factor that was not considered in the 3D city modeling process of this study.

Future research should prioritize the development of an optimized algorithm capable of modeling existing buildings up to LOD4. This advancement would allow for more accurate estimations of individual building potential, considering detailed façades and roof features.

The prevalence of high vegetation in residential areas was a significant focus of this study. Our findings indicate that tall trees can cast substantial shadows on smaller structures, as depicted in Figures 10 and 11. These observations suggest that regions with tall and densely packed trees have a more significant impact on GSI compared to residential zones with smaller buildings, as they create substantial shading and reduce incoming solar

irradiation. The influence of these factors on solar energy production, space conditioning, and air temperature reduction requires further exploration; see Allen et al. [76].

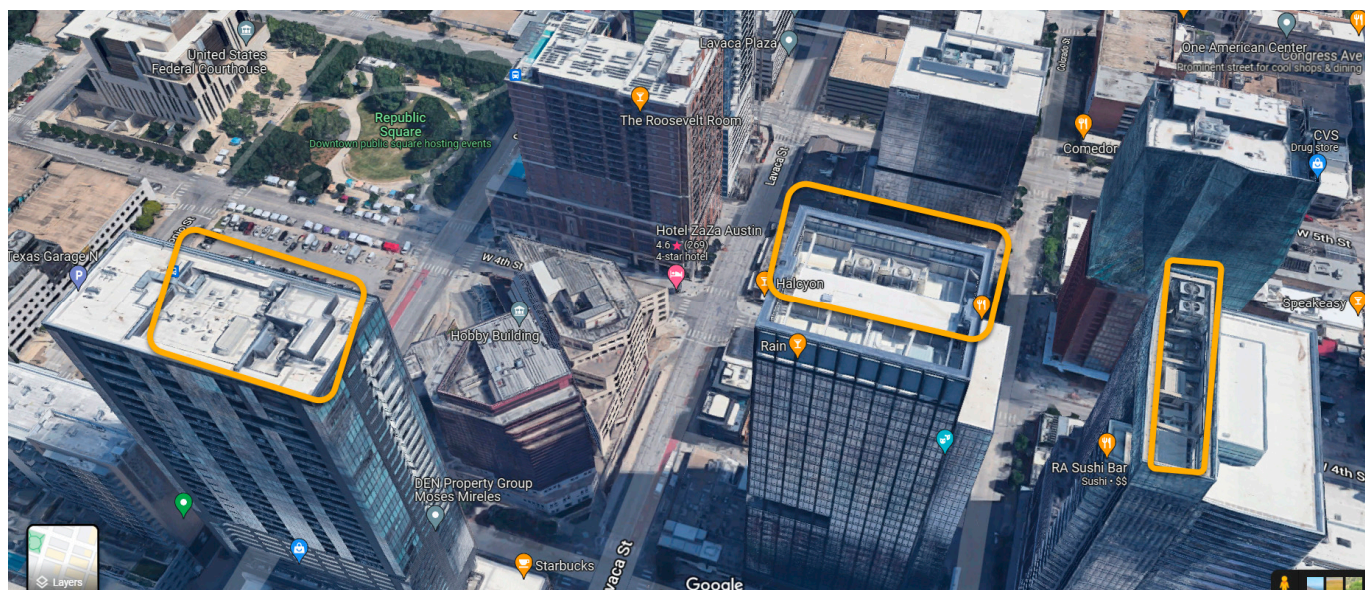


**Figure 13.** AC vents on rooftops, downtown Austin area (as indicated by the highlighted yellow box may have an impact on the efficiency of solar panels installation), courtesy of Google Maps.

In addition, the exportation process of 3D GIS data is substantially more challenging as compared to 2D GIS data. The 3D GIS data are more complicated in terms of 3D geometry and topology. Special care is taken when projecting data into the 3D web. As for the scope of this research work, ArcGIS Online was used to publish 3D data. ArcGIS Online and a 3D web application based on ArcGIS Pro 3.2 published data were used to show the final model. Furthermore, the visualization process can provide building-level information to users using web GIS technology. The data can be shared with different stakeholders and the public for community engagement. The final implementation and result of the research can be accessed via a 3D web application using the following link: <https://arcg.is/1fG9jjX> (accessed on 18 October 2023). The 3D web application was developed to be more user-friendly; it contains details of the monthly and yearly solar irradiation received by each building.

The 3D web application marks a significant forward step in the development of successful web-based public participation. It can make complicated information easy to understand and make it easier for stakeholders and city planners to get involved.

However, this research had some limitations. Specifically, the study primarily focused on rooftops and façade features were not considered. The DSM was not utilized as it disregards the accurate shape of the entire building [77]. Moreover, the use of the DSM often leads to an overestimation of solar irradiation, especially in densely populated areas. Furthermore, the absence of information on vertical surface features in the LiDAR input data prevented the inclusion of factors such as windows, doors, and other façade elements in the analysis. While façade features may contribute to solar activity, incorporating them into solar irradiation calculations may result in an overestimation due to their potential overestimation of the solar active area [78,79]. The primary focus of this study was on rooftops using LiDAR and photogrammetry, and conducting similar façade solar studies in urban contexts may present practical challenges. Additionally, there are geographical and temporal limitations in the use of atmospheric data, such as the turbidity factor and clear sky index. Factors like turbidity, sky clouds (which are difficult to predict), and reflected radiation have temporal and spatial limitations. It is essential to exercise caution while interpreting the results obtained from the Solar Analyst tool, as they provide approximate estimates of future PV potential.

## 5. Conclusions and Future Work

Our study demonstrates the importance of integrating 3D city modeling and solar potential estimation for sustainable urban planning. It enables informed decisions on PV installation, enhances renewable energy integration, fosters public engagement, and showcases geospatial technology's potential for the advancement of renewable energy solutions through interdisciplinary collaboration.

The study area in downtown Austin, Texas, heavily relies on fossil fuels like natural gas and coal to meet its energy demands. However, the burning of these fuels releases a significant amount of carbon dioxide, contributing to carbon emissions and climate change at both local and global levels. To pursue a more sustainable energy approach, SIE emerges as a viable solution.

The presence of high-rise buildings in the study area proves advantageous for PV installation, as they remain largely unaffected by shading from nearby trees. This highlights the potential for the integration of solar panels on the rooftops of these tall buildings, allowing for efficient energy generation without interference from vegetation.

In conclusion, the strategic selection of optimal locations and the adoption of innovative solar technologies can unlock the solar potential in the study area, contributing to a sustainable and eco-friendly energy future. This approach will reduce the reliance on fossil fuels, mitigate carbon emissions, and address the impacts of climate change at the local and global scales.

At the highest level of detail (LOD 4), using advanced deep learning algorithms, there is still some room for data-driven 3D city modeling, which has the potential to be highly effective in future solar planning and other geodesign processes. Due to a shortage of meteorological station data as well as other sociological and economic considerations, SIE was performed in a clear-sky environment. These factors can be included in future studies to help with the better planning of PV installation in the research area. An important consideration will be the adaptation of the model to meteorological data. This adaptation will involve the adjustment of parameters related to transmissivity and diffusive proportion. It will be necessary to conduct several modelization series to identify the optimal increments for these two parameters.

A future study may experiment with other artificial intelligence techniques and data fusion with satellite remote sensing to increase the accuracy in recognizing walls and windows in order to create a model that is more precise and accurate.

**Author Contributions:** Conceptualization, H.W. and I.M.; methodology, H.W.; software, H.W.; validation, J.S., Y.J. and F.U.K.; formal analysis, H.W.; investigation, J.S.; resources, H.W.; data curation, H.W.; writing—original draft preparation, H.W.; writing—review and editing, I.M.; visualization, F.U.K.; supervision, J.S.; project administration, Y.J.; funding acquisition, Y.J. All authors have read and agreed to the published version of the manuscript.

**Funding:** This study is supported by the National Key R&D Program of China (No. 2016YFB0502203).

**Data Availability Statement:** All data, models, and code generated or used during the study appear in the submitted article.

**Conflicts of Interest:** The authors declare no conflict of interest.

## References

1. Fogl, M.; Moudry, V. Influence of vegetation canopies on solar potential in urban environments. *Appl. Geogr.* **2016**, *66*, 73–80. [[CrossRef](#)]
2. Devabhaktuni, V.; Alam, M.; Depuru, S.S.S.R.; Green, R.C., II; Nims, D.; Near, C. Solar energy: Trends and enabling technologies. *Renew. Sustain. Energy Rev.* **2013**, *19*, 555–564. [[CrossRef](#)]
3. Waqas, H.; Shang, J.; Munir, I.; Ullah, S.; Khan, R.; Tayyab, M.; Mousa, B.G.; Williams, S. Enhancement of the energy performance of an existing building using a parametric approach. *J. Energy Eng.* **2023**, *149*, 04022057. [[CrossRef](#)]
4. Jaglin, S. Urban Electric Hybridization: Exploring the Politics of a Just Transition in the Western Cape (South Africa). *J. Urban Technol.* **2022**, *30*, 11–33. [[CrossRef](#)]

5. Akaev, A.; Davydova, O. Climate and Energy: Energy Transition Scenarios and Global Temperature Changes Based on Current Technologies and Trends. In *Reconsidering the Limits to Growth: A Report to the Russian Association of the Club of Rome*; Springer: Cham, Switzerland, 2023; pp. 53–70.
6. Jing, R.; Liu, J.; Zhang, H.; Zhong, F.; Liu, Y.; Lin, J. Unlock the hidden potential of urban rooftop agrivoltaics energy-food-nexus. *Energy* **2022**, *256*, 124626. [[CrossRef](#)]
7. Javanroodi, K.; Nik, V.M.; Mahdavinjad, M. A novel design-based optimization framework for enhancing the energy efficiency of high-rise office buildings in urban areas. *Sustain. Cities Soc.* **2019**, *49*, 101597. [[CrossRef](#)]
8. Dong, C.; Nemet, G.; Gao, X.; Barbose, G.; Sigrin, B.; O'shaughnessy, E. Machine learning reduces soft costs for residential solar photovoltaics. *Sci. Rep.* **2023**, *13*, 7213. [[CrossRef](#)] [[PubMed](#)]
9. Defaix, P.R.; van Sark, W.G.J.H.M.; Worrell, E.; de Visser, E. Technical potential for photovoltaics on buildings in the EU-27. *Sol. Energy* **2012**, *86*, 2644–2653. [[CrossRef](#)]
10. Eremia, M.; Toma, L.; Sanduleac, M. The smart city concept in the 21st century. *Procedia Eng.* **2017**, *181*, 12–19. [[CrossRef](#)]
11. Lu, Y.; Wu, Z.; Chang, R.; Li, Y. Building Information Modeling (BIM) for green buildings: A critical review and future directions. *Autom. Constr.* **2017**, *83*, 134–148. [[CrossRef](#)]
12. Avtar, R.; Tripathi, S.; Aggarwal, A.K.; Kumar, P. Population–urbanization–energy nexus: A review. *Resources* **2019**, *8*, 136. [[CrossRef](#)]
13. Hofierka, J.; Kaňuk, J. Assessment of photovoltaic potential in urban areas using open-source solar radiation tools. *Renew. Energy* **2009**, *34*, 2206–2214. [[CrossRef](#)]
14. Santos, T.; Gomes, N.; Freire, S.; Brito, M.; Santos, L.; Tenedório, J. Applications of solar mapping in the urban environment. *Appl. Geogr.* **2014**, *51*, 48–57. [[CrossRef](#)]
15. Li, Z.; Zhang, Z.; Davey, K. Estimating geographical pv potential using lidar data for buildings in downtown San Francisco. *Trans. GIS* **2015**, *19*, 930–963. [[CrossRef](#)]
16. Li, H.; Yi, H. Multilevel governance and deployment of solar PV panels in U.S. cities. *Energy Policy* **2014**, *69*, 19–27. [[CrossRef](#)]
17. Srećković, N.; Lukač, N.; Žalik, B.; Štumberger, G. Determining roof surfaces suitable for the installation of PV (photovoltaic) systems, based on LiDAR (Light Detection And Ranging) data, pyranometer measurements, and distribution network configuration. *Energy* **2016**, *96*, 404–414. [[CrossRef](#)]
18. Nutkiewicz, A.; Yang, Z.; Jain, R.K. Data-driven Urban Energy Simulation (DUE-S): A framework for integrating engineering simulation and machine learning methods in a multi-scale urban energy modeling workflow. *Appl. Energy* **2018**, *225*, 1176–1189. [[CrossRef](#)]
19. Lee, J.; Zlatanova, S. Solar radiation over the urban texture: LIDAR data and image processing techniques for environmental analysis at city scale. In *3D Geo-Information Sciences*; Springer: Heidelberg/Berlin, Germany, 2009; pp. 319–340.
20. Pili, S.; Desogus, G.; Melis, D. A GIS tool for the calculation of solar irradiation on buildings at the urban scale, based on Italian standards. *Energy Build.* **2018**, *158*, 629–646. [[CrossRef](#)]
21. Zhang, Y.; Dai, Z.; Wang, W.; Li, X.; Chen, S.; Chen, L. Estimation of the Potential Achievable Solar Energy of the Buildings Using Photogrammetric Mesh Models. *Remote Sens.* **2021**, *13*, 2484. [[CrossRef](#)]
22. Hofierka, J.; Gallay, M.; Onačillová, K.; Hofierka, J., Jr. Physically-based land surface temperature modeling in urban areas using a 3-D city model and multispectral satellite data. *Urban Clim.* **2020**, *31*, 100566. [[CrossRef](#)]
23. Levinson, R.; Akbari, H.; Pomerantz, M.; Gupta, S. Solar access of residential rooftops in four California cities. *Sol. Energy* **2009**, *83*, 2120–2135. [[CrossRef](#)]
24. Tooke, T.R.; Coops, N.C.; Voogt, J.A.; Meitner, M.J. Tree structure influences on rooftop-received solar radiation. *Landsc. Urban Plan.* **2011**, *102*, 73–81. [[CrossRef](#)]
25. Machete, R.; Falcão, A.P.; Gomes, M.G.; Rodrigues, A.M. The use of 3D GIS to analyse the influence of urban context on buildings' solar energy potential. *Energy Build.* **2018**, *177*, 290–302. [[CrossRef](#)]
26. Han, Y.; Pan, Y.; Zhao, T.; Sun, C. Evaluating buildings' solar energy potential concerning urban context based on UAV photogrammetry. In Proceedings of the 16th IBPSA Conference, Rome, Italy, 2–4 September 2019; pp. 3610–3617.
27. Mansouri Kouhestani, F.; Byrne, J.; Johnson, D.; Spencer, L.; Hazendonk, P.; Brown, B. Evaluating solar energy technical and economic potential on rooftops in an urban setting: The city of Lethbridge, Canada. *Int. J. Energy Environ. Eng.* **2019**, *10*, 13–32. [[CrossRef](#)]
28. Huang, X.; Hayashi, K.; Matsumoto, T.; Tao, L.; Huang, Y.; Tomino, Y. Estimation of Rooftop Solar Power Potential by Comparing Solar Radiation Data and Remote Sensing Data—A Case Study in Aichi, Japan. *Remote Sens.* **2022**, *14*, 1742. [[CrossRef](#)]
29. Du, Y.; Qin, B.; Zhao, C.; Zhu, Y.; Cao, J.; Ji, Y. A novel spatio-temporal synchronization method of roadside asynchronous mmw radar-camera for sensor fusion. *IEEE Trans. Intell. Transp. Syst.* **2021**, *23*, 22278–22289. [[CrossRef](#)]
30. Zhou, G.; Bao, X.; Ye, S.; Wang, H.; Yan, H. Selection of optimal building facade texture images from uav-based multiple oblique image flows. *IEEE Trans. Geosci. Remote Sens.* **2020**, *59*, 1534–1552. [[CrossRef](#)]
31. Zhou, G.; Zhou, X.; Song, Y.; Xie, D.; Wang, L.; Yan, G.; Hu, M.; Liu, B.; Shang, W.; Gong, C.; et al. Design of supercontinuum laser hyperspectral light detection and ranging (LiDAR) (SCLaHS LiDAR). *Int. J. Remote Sens.* **2021**, *42*, 3731–3755. [[CrossRef](#)]
32. Newman, C.; Edwards, D.; Martek, I.; Lai, J.; Thwala, W.D.; Rillie, I. Industry 4.0 deployment in the construction industry: A bibliometric literature review and UK-based case study. *Smart Sustain. Built Environ.* **2020**, *10*, 557–580. [[CrossRef](#)]

33. Prieto, A.; Knaack, U.; Auer, T.; Klein, T. Solar coolfacades: Framework for the integration of solar cooling technologies in the building envelope. *Energy* **2017**, *137*, 353–368. [[CrossRef](#)]
34. Sun, R.; Wang, J.; Cheng, Q.; Mao, Y.; Ochieng, W.Y. A new IMU-aided multiple GNSS fault detection and exclusion algorithm for integrated navigation in urban environments. *GPS Solut.* **2021**, *25*, 147. [[CrossRef](#)]
35. Gröger, G.; Plümer, L. CityGML–Interoperable semantic 3D city models. *ISPRS J. Photogramm. Remote Sens.* **2012**, *71*, 12–33. [[CrossRef](#)]
36. Nys, G.; Billen, R. From consistency to flexibility: A simplified database schema for the management of CityJSON 3D city models. *Trans. GIS* **2021**, *25*, 3048–3066. [[CrossRef](#)]
37. Wieland, M.; Nichersu, A.; Murshed, S.M.; Wendel, J. Computing solar radiation on CityGML building data. In Proceedings of the 18th AGILE International Conference on Geographic Information Science, National Harbor, MD, USA, 3–7 August 2015.
38. Li, X.; Ratti, C. Mapping the spatio-temporal distribution of solar radiation within street canyons of Boston using Google Street View panoramas and building height model. *Landsc. Urban Plan.* **2019**, *191*, 103387. [[CrossRef](#)]
39. Gong, F.-Y.; Zeng, Z.-C.; Ng, E.; Norford, L.K. Spatiotemporal patterns of street-level solar radiation estimated using Google Street View in a high-density urban environment. *J. Affect. Disord.* **2019**, *148*, 547–566. [[CrossRef](#)]
40. Zhang, X.; Lv, Y.; Tian, J.; Pan, Y. An integrative approach for solar energy potential estimation through 3D modeling of buildings and trees. *Can. J. Remote Sens.* **2015**, *41*, 126–134. [[CrossRef](#)]
41. Adjiski, V.; Kaplan, G.; Mijalkovski, S. Assessment of the solar energy potential of rooftops using LiDAR datasets and GIS based approach. *Int. J. Eng. Geosci.* **2022**, *8*, 188–199. [[CrossRef](#)]
42. Abd Latif, Z.; Zaki, N.A.M.; Salleh, S.A. GIS-based estimation of rooftop solar photovoltaic potential using LiDAR. In Proceedings of the 2012 IEEE 8th International Colloquium on Signal Processing and Its Applications, Malacca, Malaysia, 23–25 March 2012; pp. 388–392.
43. Taminau, J.; Byrne, J.; Kim, J.; Kim, M.; Seo, J. Inferential-and measurement-based methods to estimate rooftop “solar city” potential in megacity Seoul, South Korea. *Wiley Interdiscip. Rev. Energy Environ.* **2022**, *11*, e438. [[CrossRef](#)]
44. Jakica, N. State-of-the-art review of solar design tools and methods for assessing daylighting and solar potential for building-integrated photovoltaics. *Renew. Sustain. Energy Rev.* **2018**, *81*, 1296–1328. [[CrossRef](#)]
45. Hofierka, J.; Zlocha, M. A new 3-D solar radiation model for 3-D city models. *Trans. GIS* **2012**, *16*, 681–690. [[CrossRef](#)]
46. Feijoo, F.; Iyer, G.C.; Avraam, C.; Siddiqui, S.A.; Clarke, L.E.; Sankaranarayanan, S.; Binsted, M.T.; Patel, P.L.; Prates, N.C.; Torres-Alfaro, E.; et al. The future of natural gas infrastructure development in the United states. *Appl. Energy* **2018**, *228*, 149–166. [[CrossRef](#)]
47. Lei, R.; Feng, S.; Lauvaux, T. Country-scale trends in air pollution and fossil fuel CO<sub>2</sub> emissions during 2001–2018: Confronting the roles of national policies and economic growth. *Environ. Res. Lett.* **2020**, *16*, 014006. [[CrossRef](#)]
48. Upadhyay, R.K. Markers for global climate change and its impact on social, biological and ecological systems: A review. *Am. J. Clim. Chang.* **2020**, *09*, 159–203. [[CrossRef](#)]
49. Yu, J.; Tang, Y.M.; Chau, K.Y.; Nazar, R.; Ali, S.; Iqbal, W. Role of solar-based renewable energy in mitigating CO<sub>2</sub> emissions: Evidence from quantile-on-quantile estimation. *Renew. Energy* **2022**, *182*, 216–226. [[CrossRef](#)]
50. Kutzner, T.; Chaturvedi, K.; Kolbe, T.H. CityGML 3.0: New functions open up new applications. *PFG–J. Photogramm. Remote Sens. Geoinf. Sci.* **2020**, *88*, 43–61. [[CrossRef](#)]
51. Biljecki, F.; Ledoux, H.; Stoter, J. Does a finer level of detail of a 3D city model bring an improvement for estimating shadows. In *Advances in 3D Geoinformation*; Springer: Heidelberg/Berlin, Germany, 2017; pp. 31–47.
52. Dukai, B.; Ledoux, H.; Stoter, J.E. A multi-height LoD1 model of all buildings in the Netherlands. *ISPRS Ann. Photogramm. Remote Sens. Spat. Inf. Sci.* **2019**, *4*, 51–57. [[CrossRef](#)]
53. Pijl, A.; Bailly, J.-S.; Feurer, D.; El Maaoui, M.A.; Boussema, M.R.; Tarolli, P. TERRA: Terrain extraction from elevation rasters through repetitive anisotropic filtering. *Int. J. Appl. Earth Obs. Geoinf.* **2020**, *84*, 101977. [[CrossRef](#)]
54. Shabbir, A.; Ali, N.; Ahmed, J.; Zafar, B.; Rasheed, A.; Sajid, M.; Ahmed, A.; Dar, S.H. Satellite and scene image classification based on transfer learning and fine tuning of ResNet50. *Math. Probl. Eng.* **2021**, *2021*, 5843816. [[CrossRef](#)]
55. Zhao, K.; Kang, J.; Jung, J.; Sohn, G. Building extraction from satellite images using mask R-CNN with building boundary regularization. In Proceedings of the IEEE Computer Society Conference on Computer Vision and Pattern Recognition Workshops, Salt Lake City, UT, USA, 18–22 June 2018; pp. 247–251.
56. Maharana, K.; Mondal, S.; Nemade, B. A review: Data pre-processing and data augmentation techniques. *Glob. Transit. Proc.* **2022**, *3*, 91–99. [[CrossRef](#)]
57. Sakeena, M.; Stumpe, E.; Despotovic, M.; Koch, D.; Zeppelzauer, M. On the Robustness and Generalization Ability of Building Footprint Extraction on the Example of SegNet and Mask R-CNN. *Remote Sens.* **2023**, *15*, 2135. [[CrossRef](#)]
58. Nath, N.D.; Chaspari, T.; Behzadan, A.H. Single- and multi-label classification of construction objects using deep transfer learning methods. *J. Inf. Technol. Constr.* **2019**, *24*, 511–526. [[CrossRef](#)]
59. Gupta, S.; Weinacker, H.; Koch, B. Comparative analysis of clustering-based approaches for 3-d single tree detection using airborne fullwave lidar data. *Remote Sens.* **2010**, *2*, 968–989. [[CrossRef](#)]
60. Liang, J.; Gong, J.; Zhou, J.; Ibrahim, A.N.; Li, M. An open-source 3D solar radiation model integrated with a 3D Geographic Information System. *Environ. Model. Softw.* **2015**, *64*, 94–101. [[CrossRef](#)]

61. Bode, C.A.; Limm, M.P.; Power, M.E.; Finlay, J.C. Subcanopy Solar Radiation model: Predicting solar radiation across a heavily vegetated landscape using LiDAR and GIS solar radiation models. *Remote Sens. Environ.* **2014**, *154*, 387–397. [[CrossRef](#)]
62. Massimo, A.; Dell’Isola, M.; Frattolillo, A.; Ficco, G. Development of a geographical information system (GIS) for the integration of solar energy in the energy planning of a wide area. *Sustainability* **2014**, *6*, 5730–5744. [[CrossRef](#)]
63. Fu, P.; Rich, P.M. Design and Implementation of the Solar Analyst: An ArcView Extension for Modeling Solar Radiation at Landscape Scales. In Proceedings of the 1999 Esri User Conference Proceedings, San Diego, CA, USA, 27–30 July 1999; pp. 1–24.
64. Kausika, B.B.; van Sark, W.G.J.H.M. Calibration and validation of ArcGIS solar radiation tool for photovoltaic potential determination in the Netherlands. *Energies* **2021**, *14*, 1865. [[CrossRef](#)]
65. Quirós, E.; Pozo, M.; Ceballos, J. Solar potential of rooftops in Cáceres city, Spain. *J. Maps* **2018**, *14*, 44–51. [[CrossRef](#)]
66. Rich, P.M. Characterizing plant canopies with hemispherical photographs. *Remote Sens. Rev.* **1990**, *5*, 3–29. [[CrossRef](#)]
67. Enjavi-Arsanjani, M.; Hirbodi, K.; Yaghoubi, M. Solar energy potential and performance assessment of CSP plants in different areas of Iran. *Energy Procedia*. **2015**, *69*, 2039–2048. [[CrossRef](#)]
68. Orte, F.; Lusi, A.; Carmona, F.; D’Elia, R.; Faramiñán, A.; Wolfram, E. Comparison of NASA-POWER solar radiation data with ground-based measurements in the south of South America. In Proceedings of the 2021 XIX Workshop on Information Processing and Control (RPIC), San Juan, Argentina, 3–5 November 2021; pp. 1–4.
69. Teyabeen, A.A.; Elhatmi, N.B.; Essnid, A.A.; Mohamed, F. Estimation of monthly global solar radiation over twelve major cities of Libya. *Energy Built Environ.* **2022**, *5*, 46–57. [[CrossRef](#)]
70. Kowe, P.; Mutanga, O.; Odindi, J.; Dube, T. Exploring the spatial patterns of vegetation fragmentation using local spatial autocorrelation indices. *J. Appl. Remote Sens.* **2019**, *13*, 024523. [[CrossRef](#)]
71. Getis, A.; Ord, J.K. The analysis of spatial association by use of distance statistics. In *Perspectives on Spatial Data Analysis*; Springer: Berlin/Heidelberg, Germany, 2010; pp. 127–145.
72. Brito, M.C.; Redweik, P.; Catita, C.; Freitas, S.; Santos, M. 3D solar potential in the urban environment: A case study in Lisbon. *Energies* **2019**, *12*, 3457. [[CrossRef](#)]
73. Lobaccaro, G.; Croce, S.; Vettorato, D.; Carlucci, S. A holistic approach to assess the exploitation of renewable energy sources for design interventions in the early design phases. *Energy Build.* **2018**, *175*, 235–256. [[CrossRef](#)]
74. Prieto, I.; Izkara, J.L.; Usobiaga, E. The application of LiDAR data for the solar potential analysis based on urban 3D model. *Remote Sens.* **2019**, *11*, 2348. [[CrossRef](#)]
75. Sredenšek, K.; Štumberger, B.; Hadžiselimović, M.; Mavsar, P.; Seme, S. Physical, geographical, technical, and economic potential for the optimal configuration of photovoltaic systems using a digital surface model and optimization method. *Energy* **2022**, *242*, 122971. [[CrossRef](#)]
76. Allen, A.; Henze, G.; Baker, K.; Pavlak, G. Evaluation of low-exergy heating and cooling systems and topology optimization for deep energy savings at the urban district level. *Energy Convers. Manag.* **2020**, *222*, 113106. [[CrossRef](#)]
77. Zhong, Q.; Nelson, J.R.; Tong, D.; Grubestic, T.H. A spatial optimization approach to increase the accuracy of rooftop solar energy assessments. *Appl. Energy* **2022**, *316*, 119128. [[CrossRef](#)]
78. Brito, M.; Freitas, S.; Guimarães, S.; Catita, C.; Redweik, P. The importance of facades for the solar PV potential of a Mediterranean city using LiDAR data. *Renew. Energy* **2017**, *111*, 85–94. [[CrossRef](#)]
79. Lindberg, F.; Jonsson, P.; Honjo, T.; Wästberg, D. Solar energy on building envelopes—3D modelling in a 2D environment. *Sol. Energy* **2015**, *115*, 369–378. [[CrossRef](#)]

**Disclaimer/Publisher’s Note:** The statements, opinions and data contained in all publications are solely those of the individual author(s) and contributor(s) and not of MDPI and/or the editor(s). MDPI and/or the editor(s) disclaim responsibility for any injury to people or property resulting from any ideas, methods, instructions or products referred to in the content.